Mon. Not. R. Astron. Soc. **000**, 000–000 (0000) Printed 20 April 2009 (MN LATEX style file v2.2)

X-ray section only of DoAr 21 paper, Jensen et al.

David H. Cohen[1⋆]
[1] *Swarthmore College, Department of Physics and Astronomy, Swarthmore, Pennsylvania 19081, USA*

20 April 2009

ABSTRACT

Note: This is simply a draft of the X-ray section of the DoAr 21 paper.

1 INTRODUCTION

2 STELLAR PROPERTIES

3 X-RAY EMISSION

DoAr 21 is the brightest X-ray source in the ρ Oph cloud core A, with an X-ray luminosity of nearly 10^{32} ergs s^{-1}, a hard thermal spectrum, and large X-ray flares seen in several archival observations at a rate of nearly one per day. Its X-ray emission has been observed at low resolution with *Einstein* (Montmerle et al. 1983), *ASCA* (Casanova et al. 1995), *ROSAT* (Koyama et al. 1994), and *Chandra* (Imanashi et al. 2002; Gagné et al. 2004).

The new *Chandra* grating spectra we present here have vastly superior spectral resolution compared to any of these previous datasets, enabling us to extract temperature and abundance information with more reliability and also, for the first time, to examine density diagnostics. Given the high rate of flaring seen in previous observations, it is not surprising that we detected a large and well-resolved flare in our 91 ksec *Chandra* observation. We can bring many of these same diagnostic tools to bear on the different portions of the new dataset - pre-flare, flare, and post-flare.

The High Energy Transmission Grating Spectrometer (HETGS) has two grating arrays – the Medium Energy Grating (MEG) with a FWHM resolution of 2.3 mÅ, and the High Energy Grating (HEG) with a resolution of 1.2 mÅ (Canizares et al. 2005). Both grating arrays operate together, with the dispersed spectra (first, second, and third orders) as well as the zeroth order spectrum recorded on the ACIS CCD array. We used standard CIAO (v.3.3) tools to extract the dispersed spectra, and to create observation specific spectral response matrices (rmfs) and effective area tabulations (garfs), as well as to create light curves (and spectra for each of the three subsets of the observation). Of the dispersed spectra, only the first order spectra have a significant number of counts. The zeroth order spectrum is severely piled up, so we restrict the analysis we report on here to the first order MEG and HEG spectra. We performed most of the spectral analysis using XSPEC v.12.3.

The goal of this X-ray spectral and timing analysis is to characterize the properties of the hot plasma on this very magnetically active pre-main-sequence star, and compare its properties to those measured in other PMS stars with high-resolution X-ray spectra. Its extreme youth and lack of obvious signatures of accretion make for an interesting contrast between DoAr 21 and the strongly accreting T Tauri stars that have been well-studied with the *Chandra* gratings (Güdel & Telleschi 2007). Although DoAr 21 is not a classical T Tauri star, it does – as we have detailed in the previous section – have some circumstellar material in its vicinity. And the observed X-rays, and the unobservable far- and extreme-UV emission associated with the X-ray emitting plasma as it cools, could have an important effect on this circumstellar material, perhaps being the dominant source of excitation for the PAH emission we reported on in the previous section. So, characterizing the X-ray properties of the star are important for understanding the physical conditions in the circumstellar environment. (*Co-authors: How's this paragraph now?*)

In Fig. 1 we show the MEG and HEG spectra (negative and positive first orders coadded in both cases), with emission lines identified and labeled. Although the *Chandra* gratings and detector have significant response to wavelengths above 30 Å, interstellar attenuation (due to photoelectric absorption, which has a cross section that goes roughly as λ^3) makes the spectrum above 12 Å nearly devoid of counts. These spectra are dominated by a strong bremsstrahlung continuum, which is indicative of plasma with a dominant temperature well in excess of 20 million K (so that atoms are mostly fully stripped and their associated line emission is weak). The presence of emission from high ion stages – up to helium-like Fe XXV and possibly even Fe XXVI – also indicates very high plasma temperatures. We analyze the temperature distribution in the plasma in detail below, both by fitting thermal emission models to the entire spectrum and also by looking at ratios of lines arising from adjacent ionization states of the same element.

3.1 Time Variability

A large flare was seen in the middle of the *Chandra* observation, with a rapid rise of about six thousand seconds, followed by an exponential decay that also shows evidence for reheating. (*Co-authors: Can we really say that the decay is exponential? Seems to me that's just a (reasonable) assumption. By the way, by my calculation - count rate falling from 0.62 to 0.40 in 13 ks, the e-folding decay time of the flare, if it is exponential, is 30 ks. Think we should say that in the paper?*) The temporal behavior is shown in Fig. 2, where we also display light curves for the hard and soft bands separately. Significant hardening is seen during the flare, which dissipates through the post-flare phase. We will first discuss fits to the total spectrum collected during the 94 ks observation. We will then discuss fits to separate spectra, formed from the pre-flare (0 through 48 ks) section of the observation, the flare (54 to 70 ks) section, and the post-flare (70 to 94 ks) section. These temporal divisions are indicated by the vertical lines in the top panel of Fig. 2.

Co-authors: David still has to (1) experiment with different wavelength cut-offs between the hard and soft bands for the light curve figure and (2) try plotting the hardness ratio directly. We can also try different binning.

3.2 Spectral Modeling

We fit the MEG and HEG first order dispersed spectra simultaneously (but not co-added) over the spectral ranges where each has a significant number of counts. For the MEG this was 2 to 12.5 Å, and for the HEG it was 1.5 to 11.5 Å. We fit a two-temperature optically thin thermal emission model (the *bapec* implementation of the Astrophysical Plasma Emission Code (APEC) (Smith et al. 2001)) that accounts for bremsstrahlung and line emission from a plasma in statistical equilibrium. This model has four free parameters: the plasma temperature, the abundances (expressed as a fraction of solar), the emission measure (proportional to the normalization of the model, and formally given by $4\pi d^2 \int n_e n_H \mathrm{d}V$, where the volume integral is of the product of the electron and proton number densities), and the line broadening (an ad hoc turbulent velocity added in quadrature to the thermal velocity of each line in the model). We also include interstellar attenuation, with cross sections from Morrison & McCammon (1983). We used the χ^2 statistic

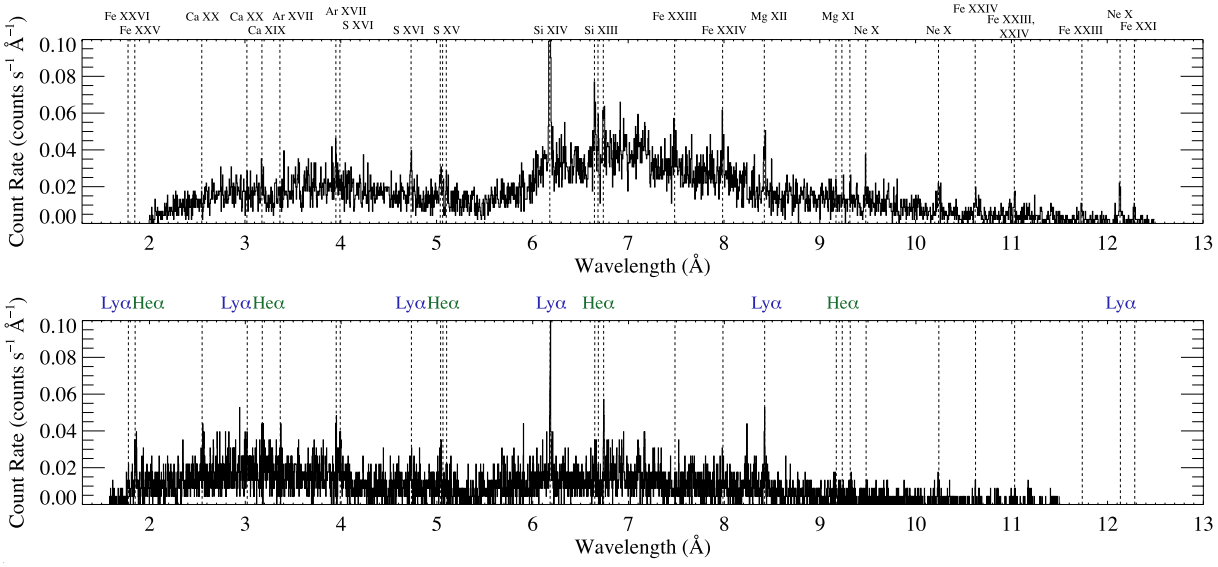

Figure 1. The entire usable portions of the MEG (top) and HEG (bottom) coadded (negative and positive) first order spectra of DoAr 21. The binning is native (2.5 mÅ for the HEG and 5 mÅ for the MEG). The shape of the continuum is dominated by the wavelength-dependent effective area of the telescope, gratings, and detector, rather than the intrinsic emission. Vertical dashed lines represent the laboratory rest wavelengths of important lines. The annotations above the top panel indicate the element and ionization stage of each line, while those above the lower panel highlight the Lyman-α lines of the hydrogen-like isoelectronic sequence and the principle transition of the helium-like isoelectronic sequence.

with Churazov weighting to assess goodness of fit and to place confidence limits on the derived model parameters.

A single temperature model does not provide a good fit, though the low resolution *ROSAT* and *Chandra* ACIS data, are adequately fit by a single temperature thermal model (Imanashi et al. 2002). We did find a good fit when we used a two temperature *bapec* model with interstellar absorption. The best-fit model has temperatures of roughly 12 and 48 million K (MK), with approximately five times the emission measure in the hotter component as in the cooler component. The abundances are sub-solar, and no significant line broadening is found, with a 68 percent confidence limit of $\sigma_{turb} = 50$ km s^{-1}; about one-third of the peak spectral resolution. We find an interstellar column density of slightly more than 10^{22} cm^{-2}, which is completely consistent with the extinction of $A_V = 6.2$ magnitudes, given the conversion between extinction and hydrogen column density of Vuong et al. (2003). The model has a flux on the range 0.3 to 10 keV of 1.48×10^{-11} ergs s^{-1} cm^{-2}. Correcting for interstellar attenuation, the unabsorbed X-ray flux is a little more than twice this. The best-fit model parameters and their 68 percent confidence limits are listed in Table 1. This fit is formally good, although the two temperatures certainly are an approximation to a continuous distribution of temperatures. Furthermore, the confidence limits are based only on statistical errors on the data, and in our experience, for datasets with many bins (the data we fit here have 12,196 bins), formal confidence limits are unrealistically tight.

Co-authors: The abundances derived from the apec model fitting are only marginally consistent among the three sectors of the observation. Pre- and post-flare differ by just 1 sigma, flare and post-flare by slightly more than 1 sigma, but the pre-flare and flare sections have abundances that differ by several sigma (the error bars on the pre-flare abundances are unrealistically tight in my opinion) – and in general, I'm not sure how much stock I'd put in the relatively tight error bars in general. Do you think we should at least point out this ostensible abundance trend? I do, for now, below.... I should also probably figure out what xspec was using as the reference solar abundances...

To test the robustness of this fit, we refit the data using the ISIS X-ray analysis package (v.xx)(ref? – *Marc?*). We used the APEC model with interstellar absorption, and – as we did with the fits in XSPEC – found that a two temperature model was required to achieve a good fit. The temperatures of the best-fit components were both higher by about 20 percent, and the emission measure weighting was even more skewed toward the hot component. The interstellar column density was about 10 percent lower than in the XSPEC fit. There were some differences in the method used for the fitting in ISIS, including the use of adaptive smoothing (to ensure a minimum signal to noise per bin) and a fit performed over a slightly different wavelength range. Perhaps these factor of ten or twenty percent discrepancies between the two model fitting programs are a more realistic representation of the parameter uncertainties than are the formal, statistical confidence limits. We will use the APEC model fitting in XSPEC as the standard throughout the rest of the paper.

(*Co-authors: I would like to include the wavelength range over which the data were fit in ISIS. Is it OK that we don't include the ISIS fit results quantitatively, in a table? I kind of like the ISIS vs. XSPEC comparison as a measure of parameter uncertainty. But they use the same underlying model. Are we surprised that the agreement isn't better?*)

The best-fit model, with parameters listed in the top row of Table 1, does seem to reproduce all portions of the spectrum quite well, with few systematic deviations. The

Table 1. APEC model fits

	kT_1 (keV)	EM_1 (10^{53} cm^{-3})	kT_2 (keV)	EM_2 (10^{53} cm^{-3})	Abund	$N_{\rm H}(ISM)$ (10^{22} cm^{-2})	Luminosity 10^{31} ergs s^{-1}
total	$1.00^{+.04}_{-.03}$	$6.82^{+.82}_{-.69}$	$4.16 \pm .11$	$3.07^{+.06}_{-.07}$	$0.39 \pm .02$	$1.19^{+.03}_{-.04}$	5.44
pre-flare	$0.95^{+.05}_{-.06}$	$7.40^{+1.37}_{-1.19}$	$3.10^{+.14}_{-.13}$	$21.8^{+0.9}_{-1.1}$	$0.26 \pm .02$	$1.19^{+.03}_{-.05}$	3.49
flare	$1.58^{+.08}_{-.10}$	$18.1^{+4.3}_{-3.6}$	$7.81^{+2.22}_{-0.81}$	$40.5^{+1.9}_{-3.3}$	$0.43^{+.06}_{-.05}$	$1.18 \pm .05$	9.36
post-flare	$0.80^{+.09}_{-.05}$	$11.1^{+2.4}_{-1.6}$	$4.49^{+.24}_{-.50}$	$36.9^{+2.1}_{-1.6}$	$0.31^{+.05}_{-.04}$	$1.18^{+.06}_{-.05}$	6.78

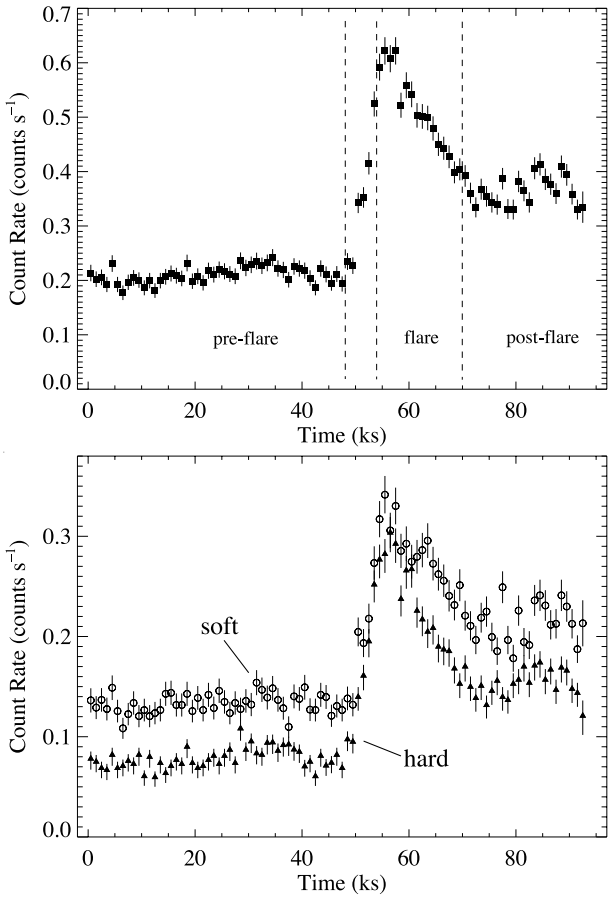

Figure 2. A light curve with 1000 second bins formed from all counts in the dispersed, first-order spectra (both MEG and HEG) (top). In the bottom panel, we show light curves made from all counts with wavelengths longer than 6 Å (open circles) and shorter than 6 Å (filled triangles). The hardening of the spectrum during the flare is evident.

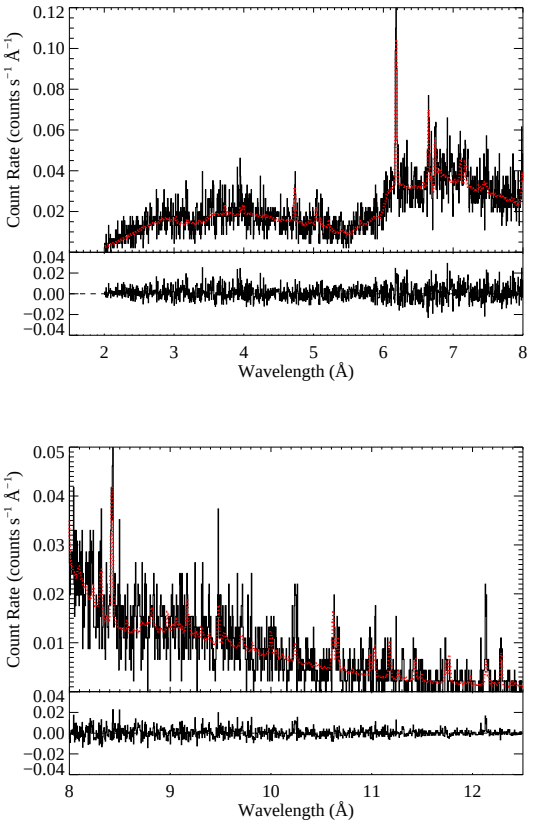

Figure 3. The best-fit two-temperature thermal emission model is superimposed (in red) on the MEG data. Fit residuals are shown below each plot. (*Co-authors: This figure will only work in color. What do you think?*)

fit to the MEG spectrum is shown in Fig. 3. The continuum is well fit, and the lines are adequately reproduced, in general. The HEG data do reveal one interesting discrepancy in this two-temperature spectral model fit, however – at the location of the He-like and H-like emission lines of iron shortward of 2 Å. These features are weak, especially the Fe XXVI emission line, but it is clear that the model predicts too much He-like relative to H-like iron emission (see Fig. 4). The iron lines seem to imply a higher temperature than the global APEC model fit does. This is likely a manifestation of a continuous temperature distribution that is only approximated by the two-temperature model we fit here. There is likely some higher temperature plasma than the 48 MK hot component we find from fitting the entire spectrum. This is in accord with the higher temperatures we derive below for the flare spectrum. The iron line emission is probably dominated by the hotter, flare plasma, whereas the overal thermal model fits are controlled by the numerous longer wavelength bins that contain much more data overall.

(*Co-authors: More subsections of the spectrum along with the best-fit model are shown here: projects/doar21/www/spectra*)

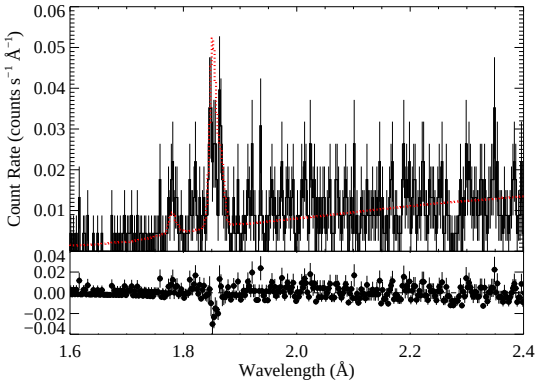

Figure 4. The best-fit two-temperature thermal emission model is superimposed (in red) on the short wavelength end of the HEG data, which includes the Lyα line of Fe XXVI at 1.78 Å and the Heα line of Fe XXV at 1.85 Å. The model fits the high-energy continuum quite well, but appears to be too cool to reproduce the observed iron line ratio. (*Co-authors: What do you think about this figure?*)

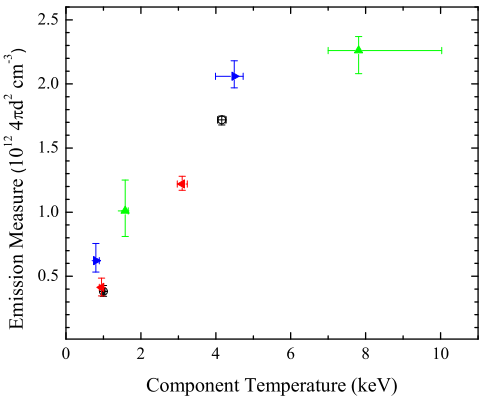

Figure 5. Summary of the parameters of the two-temperature fits to the pre-flare (red, left-pointing triangles), flare (green, upward-pointing triangles), and post-flare (blue, right-pointing triangles) data, along with the fis to the entire dataset (open circles). (*Co-authors: Maybe I should make these symbols bigger? Are they distinctive enough in b/w?*)

3.3 Spectral Analysis of the Pre-flare, Flare, and Post-flare Data

We next repeat the two-temperature thermal fitting on the pre-flare, flare, and post-flare spectra separately. The results are reported in Table 1, and summarized in Fig. 5. The temperatures and emission measures roughly double during the flare portion of the observation, with somewhat larger relative changes in the hotter component of the two-temperature model. The flare plasma temperature is in excess of 90 MK. The post-flare plasma also has a temperature distribution that is elevated with respect to the pre-flare plasma. The absorption column densities derived for each section of the observation are completely consistent with each other, which is consistent with an interestellar origin to the attenuation, as we would expect. We also note that the abundances show a marginally significant change among the three different sectors of the observation, in the sense that the hotter components – the flare and to a lesser extent the post-flare sections – have higher abundances. We are not confident that this result can be taken at face value, however, because of the unrealistically tight statistical confidence intervals one finds when fitting simplified spectral models to spectra with a very large number of bins.

3.4 Individual Emission Lines

The emission lines in the spectrum are relatively weak, but we are able to analyze the strengths of several of the srongest ones, and use them as plasma diagnostics. Specifically, the ratios of hydrogen-like to helium-like lines are temperature sensitive, and can be used to augment the temperature information from the global spectral modeling described above. Additionally, the forbidden-to-intercombination line ratios of helium-like ions are sensitive to density, as collisions depopulate the metastable upper level (^{3}S of the forbidden line), and populate the upper level ^{3}P of the intercombination line. Thus high densities (different critical densities for each element) decrease the forbidden-to-intercombination (f/i) ratio. This behavior is seen in some accreting T Tauri stars, but not in naked T Tauri or magnetically active main sequence stars.

We measured the line intensities by fitting the continuum near to each line as a flat spectrum, consistent with bremsstrahulung, and once the continuum level was established, we fit the line with a Gaussian profile model on top of the best-fit continuum level. For the closely spaced helium-like complexes, we fit all three lines simultaneously. The Si XIV/XIII and S XVI/XV ratios are $1.50^{+.33}_{-.28}$ and $0.55^{+.26}_{-.13}$, respectively. For the helium-like intensity we use the flux in the resonance, intercombination, and forbidden lines combined. We modeled the temperature dependence of these line ratios using the collisional-radiative equilibrium code, PrismSpect (ref), and find that the measured values imply temperatures of XX and YY. We also used APEC to model the temperature dependence, and got similar results.

(*Co-authors: The temperature modeling still needs to be done. And the results discussed in the context of the 2-T* APEC *modeling. We will also look at these ratios in the pre-flare, flare, and post-flare spectra, separately. To some extent, I haven't given this a high priority because I don't think the results will be that interesting - both because line ratio temperature diagnostics are kind of hokey and because the S/N in these lines will be quite poor in each of the three separate sections. Not sure if it's even worth doing this, given that the 2-T spectral modeling is pretty conclusive. Let me know what you think.*)

The f/i ratios for Si XIII and S XV are $5.4^{+2.6}_{-2.2}$ and $1.90^{+2.28}_{-.82}$, respectively. None of the lower atomic number elements have enough signal-to-noise in their helium-like emission complexes for a measurement to be made. For the Si XIII, the ratio exceeds that low-density limit[1] of $f/i = 2.3$

[1] The low density limit refers to the density below which colli-

to 2.5 with one sigma significance. This limits the density to less than $\sim 10^{12}$ cm^{-3}. The 95 percent upper confidence limit on the density is 9×10^{12} cm^{-3}. For S XV the forbidden-to-intercombination ratio is consistent with the low-density limit of $f/i = 2.0$ to 2.1. The one sigma lower limit on f/i for S XV corresponds to a density of 10^{14} cm^{-3}. The constraints are depicted in Fig. 6 and the HEG measurement of the Si XIII complex – which provides the tightest constraints – is shown in Fig. 7.

The Si XIII complex is in the low-density limit (nearly two sigma above it, in fact). This is in contrast to altered f/i ratios in accreting CTTSs. However, the altered f/i ratios in CTTSs are generally seen in lower Z elements' He-like complexes, such as Ne IX and O VII, which have lower critical densities than Si XIII. It takes higher densities to alter the Si XIII f/i ratio, and so the limits we have derived here are not especially strong. The lower Z features seen in those WTTSs, which are at longer wavelengths, are not visible in the *Chandra* spectrum of DoAr 21 because of the large amount of interestellar attenuation.

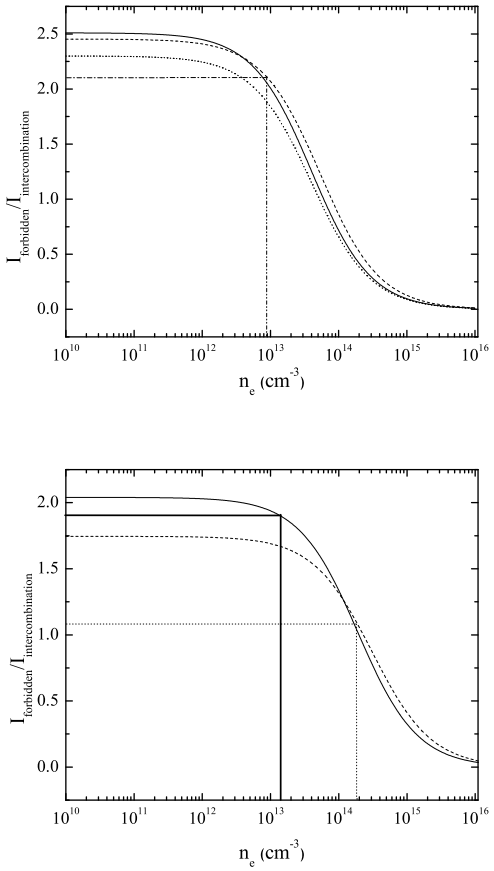

Figure 6. Models of the f/i ratios of Si XIII (top) and S XV (bottom), as a function of electron density. The models are from Blumenthal et al. (1972) (solid curve), Porquet & Dubau (2000) (dotted), and PrismSpect (dashed). In the bottom panel, the solid horizontal line represents the best-fit f/i value and the solid vertical line represents the corresponding electron density. The dash-dot lines represent the one sigma lower limit on the f/i ratio and the corresponding upper limit on the electron density. In the top panel we show only the 95 percent lower limit on f/i of 2.10 as a dash-dot line, corresponding to a 95 percent upper limit on density of $n_e = 9 \times 10^{12}$ cm^{-3}. (*Co-authors: I'd like to work some more on making these plots clearer.*)

sional excitation out of the metastable excited state of the forbidden line is unimportant compared to spontaneous emission to the ground sate. We give a range of values for the low-density f/i limit for each element. These represent the range of values found from PrismSpect calculations and from Blumenthal et al. (1972) and Porquet & Dubau (2000).

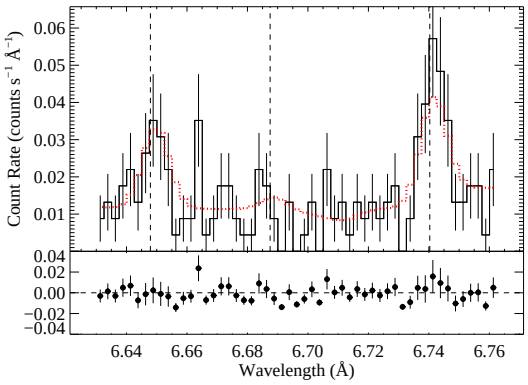

Figure 7. The Si XIII in the HEG shows a strong forbidden line (at 6.74 Å) and a weak intercombination line (at 6.68 Å), consistent with the low-density limit. (*Co-authors: should we show any of the other complexes? Comment explicitly here in the caption on the contrast with CTTSs?*)

REFERENCES

Blumenthal G.R., Drake G.W.F., Tucker W.H., 1972, ApJ, 172, 205
Canizares C.R., et al., 2005, PASP, 117, 1144
Casanova S., Montmerle T., Feigelson E. D., André P., 1995, ApJ, 439, 752
Gagné M., Skinner S. L., Daniel K. J., 2004, ApJ, 613, 393
Güdel M., Telleschi A., 2007, A&A, 474, 25
Imanishi K., Tsujimoto M., Koyama K., 2002, ApJ, 572, 300
Koyama K., Maeda Y., Ozaki M., Ueno S., Kamata Y., Wawara, Y, Sinner S., Yamauchi S., 1994, PASJ, 46, L125
Montmerle T., Koch-Miramond L., Falgarone E., Grindlay J. E., 1983, ApJ, 269, 182
Morrison R., McCammon D., 1983, ApJ, 270, 119
Porquet D.,Dubau J., 2000, A&AS, 143, 495
Smith R. K., Brickhouse N. S., Liedahl D. A., Raymond J. C., 2001, ApJ, 556, L91
Vuong M. H., Montmerle T., Grosso N., Feigelson E. D., Verstraete L., Ozawa H., 2003, A&A, 408, 581